

Supplement of The Cryosphere, 19, 1973–1993, 2025  
<https://doi.org/10.5194/tc-19-1973-2025-supplement>  
© Author(s) 2025. CC BY 4.0 License.



*Supplement of*

## **Tracing ice loss from the Late Holocene to the future in eastern Nuussuaq, central western Greenland**

**Josep Bonsoms et al.**

*Correspondence to:* Juan Ignacio López-Moreno (nlopez@ipe.csic.es)

The copyright of individual parts of the supplement might differ from the article licence.

## Supplementary materials

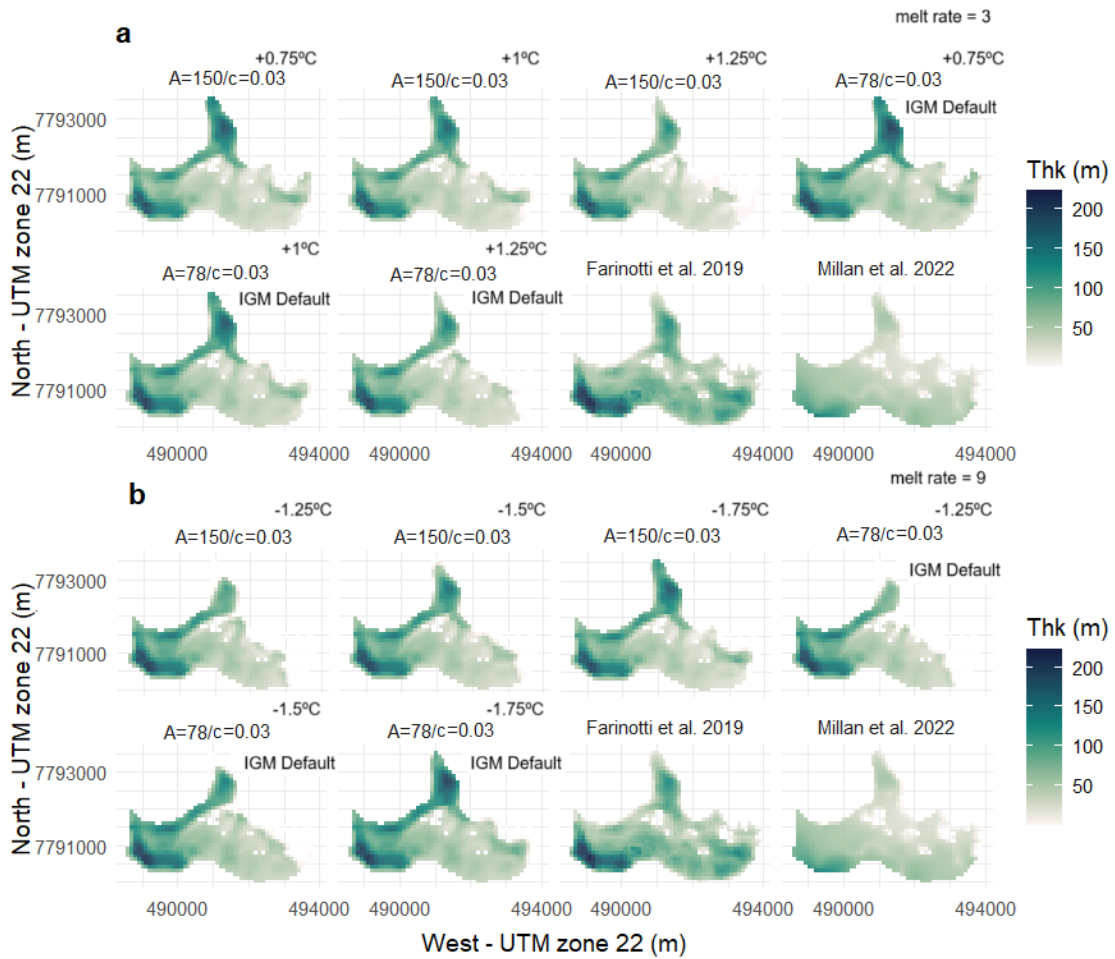


**Figure S1.** Average ice thickness data from Farinotti et al. (2019) and Millan et al. (2022) are presented alongside examples of IGM configuration options using different temperature perturbations relative to the baseline climate, as well as variations in A and c parameters. Data are shown for low (3) (a) and high-end (9) (b) melt rates. The ice thickness values obtained from IGM represent steady-state glacier conditions after a 1000-year model run.

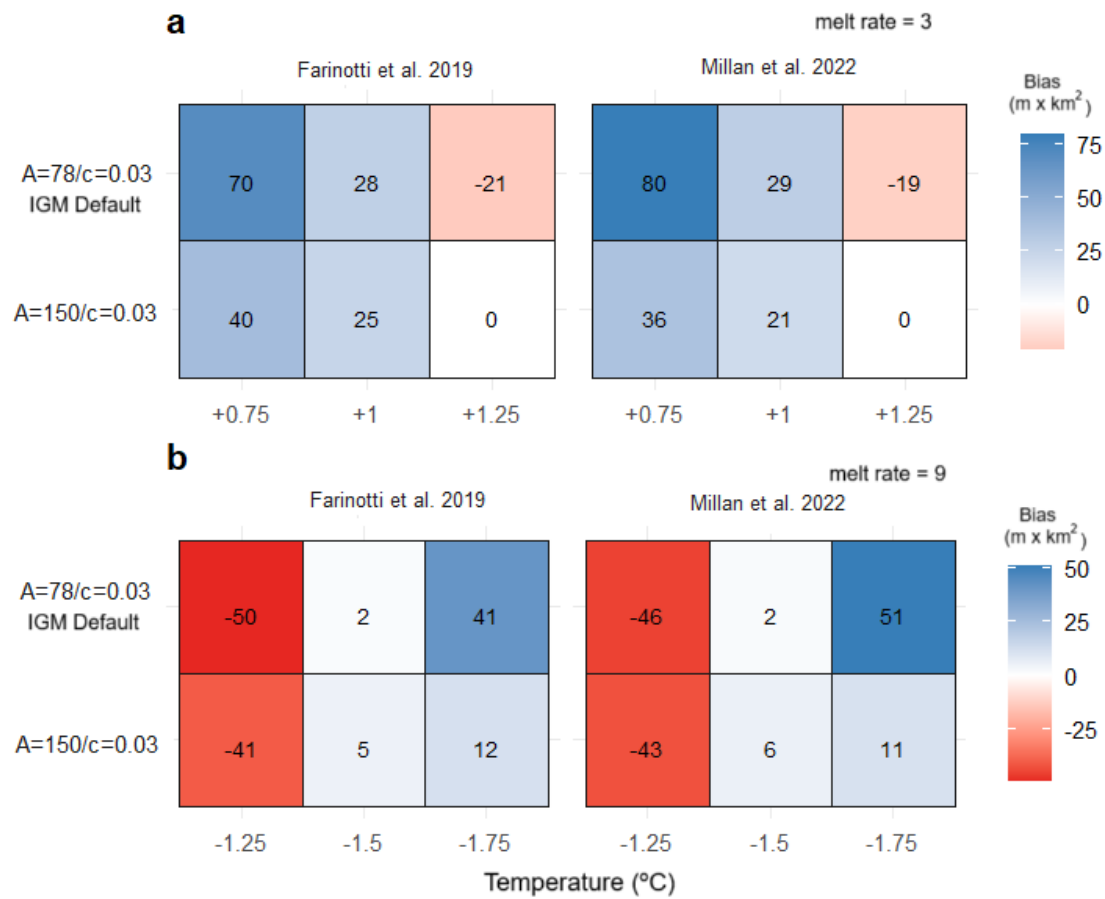


**Figure S2.** Ice thickness MAE values were multiplied by the difference between the RGI6.0 area and the IGM outputs (bias) for different A and c parameterizations and temperature perturbations. Data are shown for low (a) and high (b) melt rates, relative to ice thickness estimates from Farinotti et al. (2019) and Millan et al. (2022).

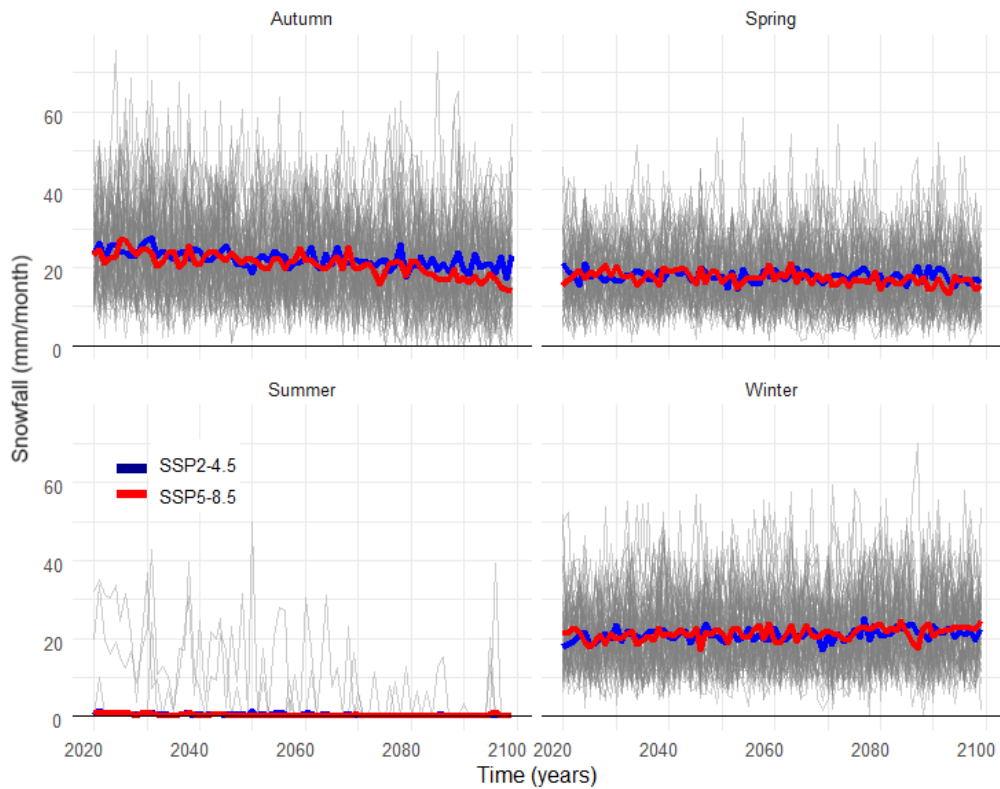


**Figure S3.** Temporal evolution of CMIP6 SSP2-4.5 and SSP5-8.5 temperature anomalies with respect to the baseline climate period grouped by season.

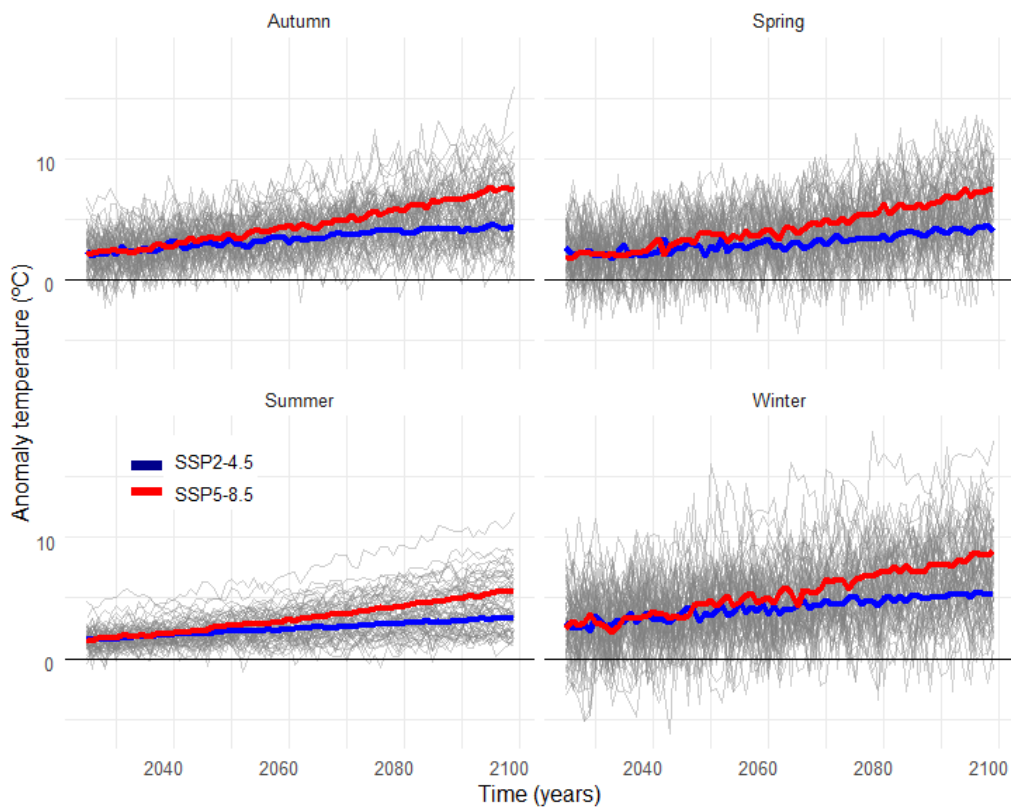


**Figure S4.** Temporal evolution of CMIP6 SSP2-4.5 and SSP5-8.5 snowfall anomalies with respect to the baseline climate period grouped by season.

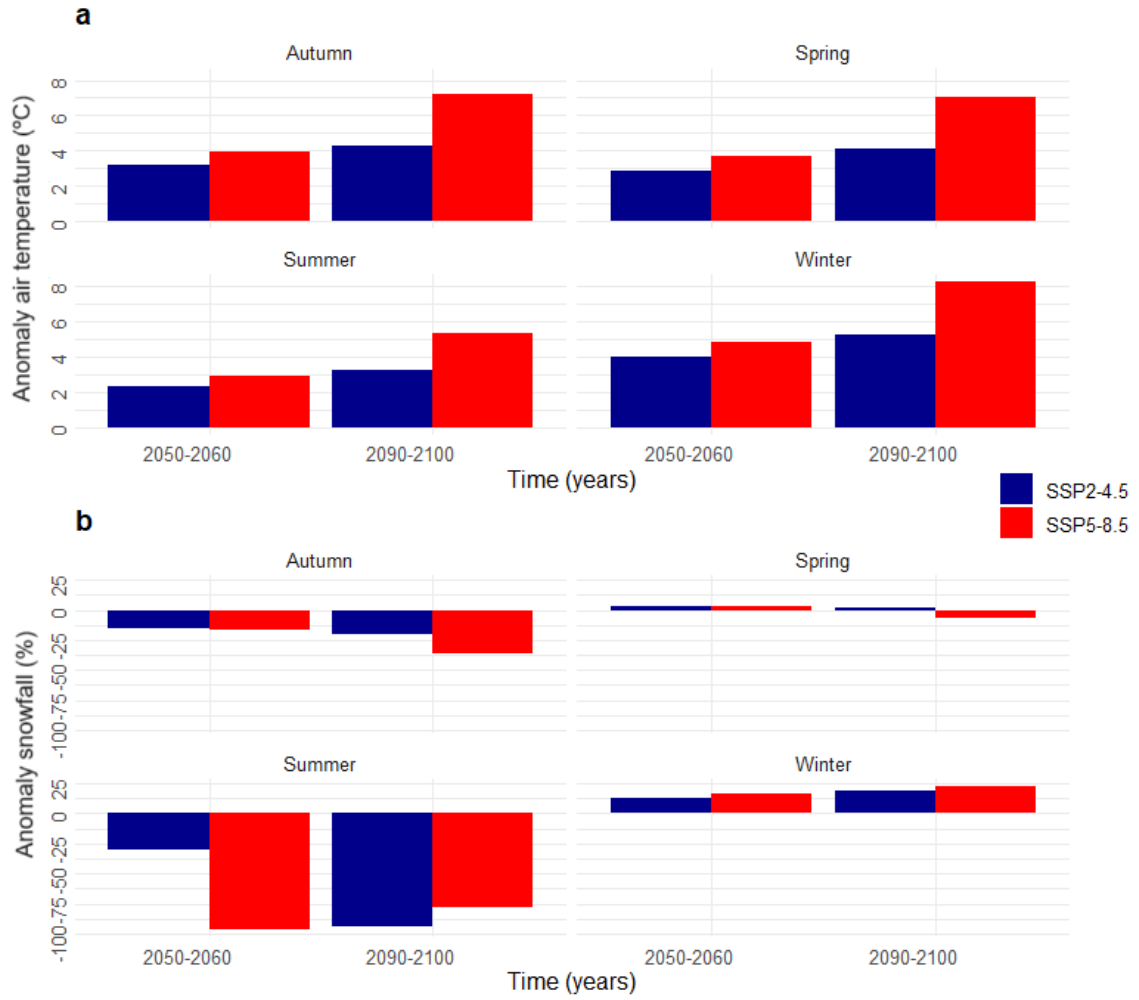


**Figure S5.** Comparison of CMIP6 SSP2-4.5 and SSP5-8.5 temperature (a) and snowfall (b) anomalies with respect to the baseline climate period for 2050-2060 and 2090-2100 temporal periods grouped by seasons.

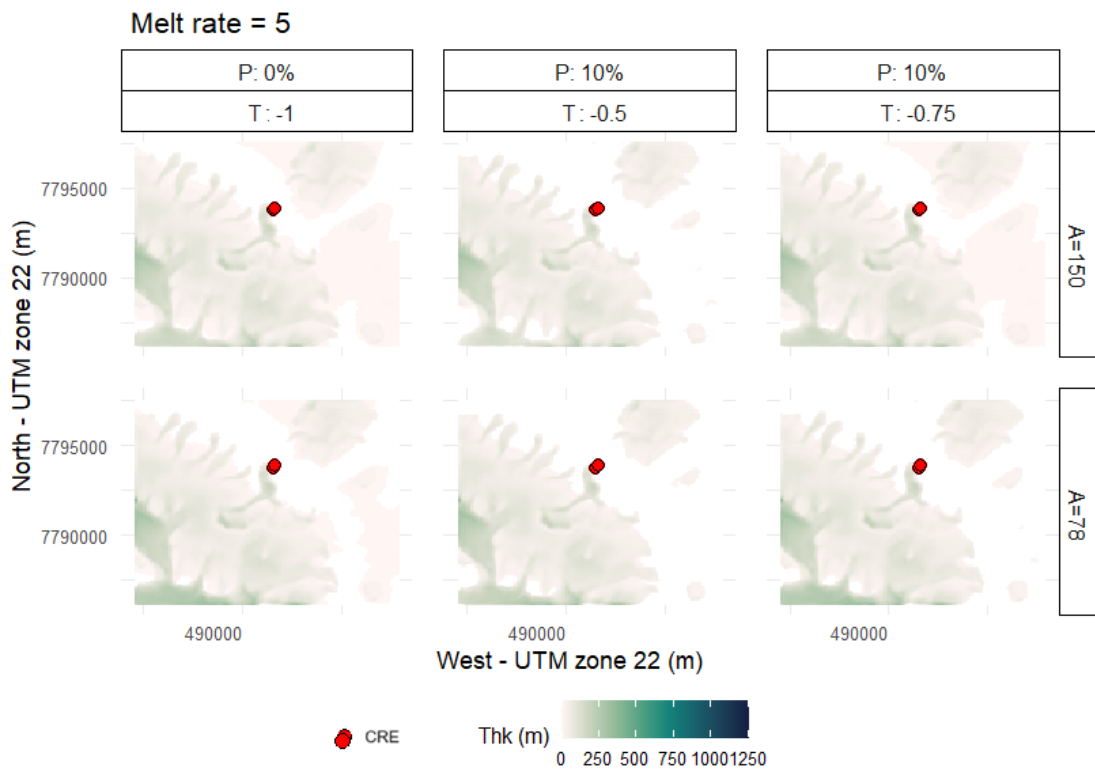


**Figure S6.** Location of the CRE samples (red dots) and average ice thickness (m) for various temperature (T) and precipitation (P) perturbations that show the best matching. The ice thickness values presented result from an initial spin-up model run, followed by a 1000-year model run to reconstruct the MIE of the Late Holocene. Data are shown for the calibrated melt rate (5) and calibrated IGM configuration ( $A = 150 \text{ MPa}^{-3} \text{ a}^{-1}$ ,  $c = 0.03 \text{ km MPa}^{-3} \text{ a}^{-1}$ ) as well as IGM default configuration ( $A = 78 \text{ MPa}^{-3} \text{ a}^{-1}$ ,  $c = 0.03 \text{ km MPa}^{-3} \text{ a}^{-1}$ ).



**Figure S7.** Location of the CRE samples (red dots) and average ice thickness (m) for various temperature (T) and precipitation (P) perturbations that show the best matching. The ice thickness values presented result from an initial spin-up model run, followed by a 1000-year model run to reconstruct the MIE of the Late Holocene. Data are shown for a low-end melt rate (3) and calibrated IGM configuration ( $A = 150 \text{ MPa}^{-3} \text{ a}^{-1}$ ,  $c = 0.03 \text{ km MPa}^{-3} \text{ a}^{-1}$ ).

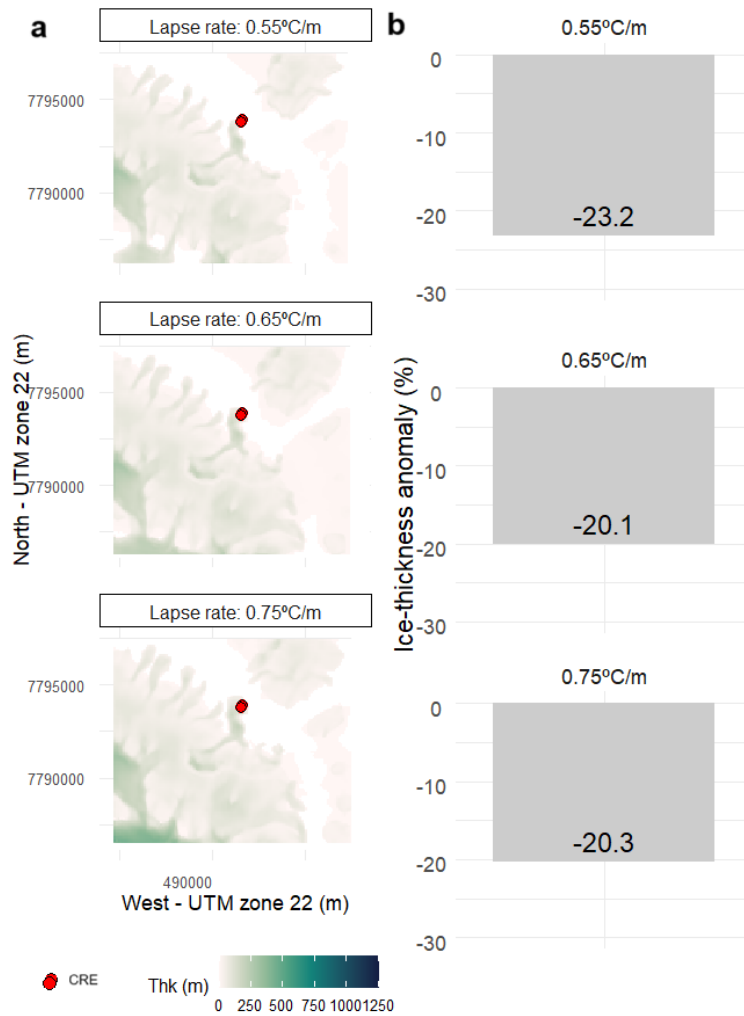


**Figure S8.** Location of the CRE samples (red dots) and average ice thickness (m) for different temperature lapse rates. The ice thickness values shown are derived from an initial spin-up model run, followed by a 1000-year simulation to reconstruct the Maximum Ice Extent (MIE) of the Late Holocene (a). The data correspond to the calibrated melt rate (5), the optimized IGM configuration ( $A = 150 \text{ MPa}^{-3} \text{ a}^{-1}$ ,  $c = 0.03 \text{ km MPa}^{-3} \text{ a}^{-1}$ ) and the best-matching air temperature perturbation validated using CRE samples. Ice thickness anomalies relative to the present-day glaciated area for the MIE of the Late Holocene under different air temperature lapse rates (b). The ice thickness anomaly is calculated as the difference between the Late Holocene MIE and the present-day accumulated yearly ice thickness. This difference is then divided by the present-day accumulated yearly ice thickness and multiplied by 100 to express the anomaly as a percentage.

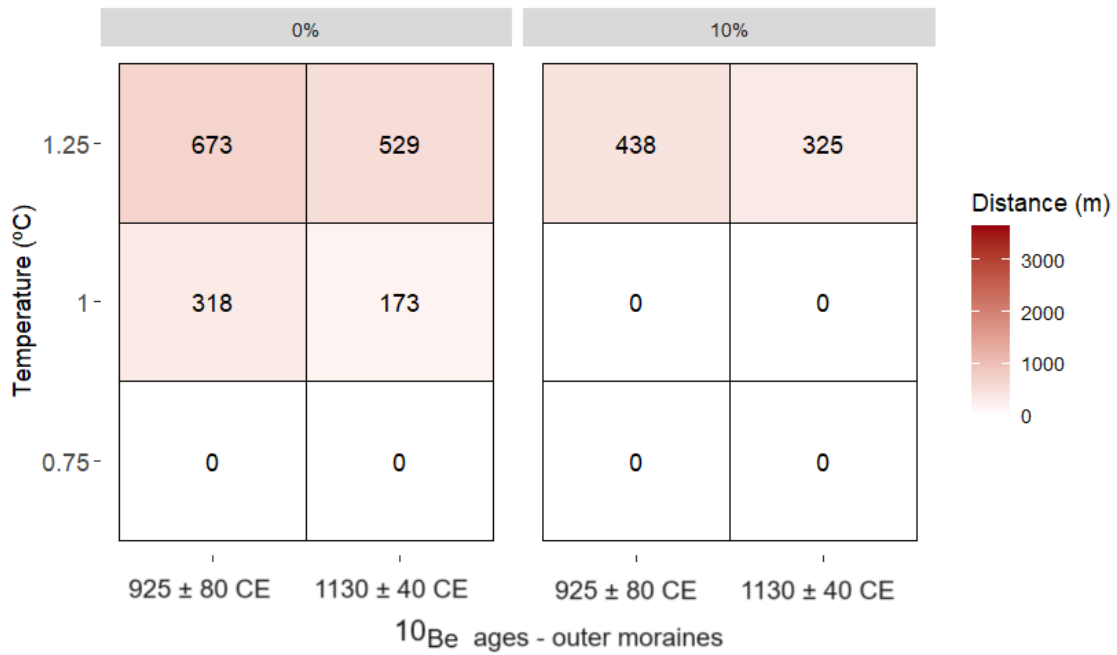


**Figure S9.** Differences in pixel distance (m) between the nearest modelled glacier extension and the sample age location (x-axis) across various air temperature (y-axis) and precipitation options (boxes). Data are shown for the calibrated IGM configuration ( $A = 150 \text{ MPa}^{-3} \text{ a}^{-1}$ ,  $c = 0.03 \text{ km MPa}^{-3} \text{ a}^{-1}$ ) and melt rate values.

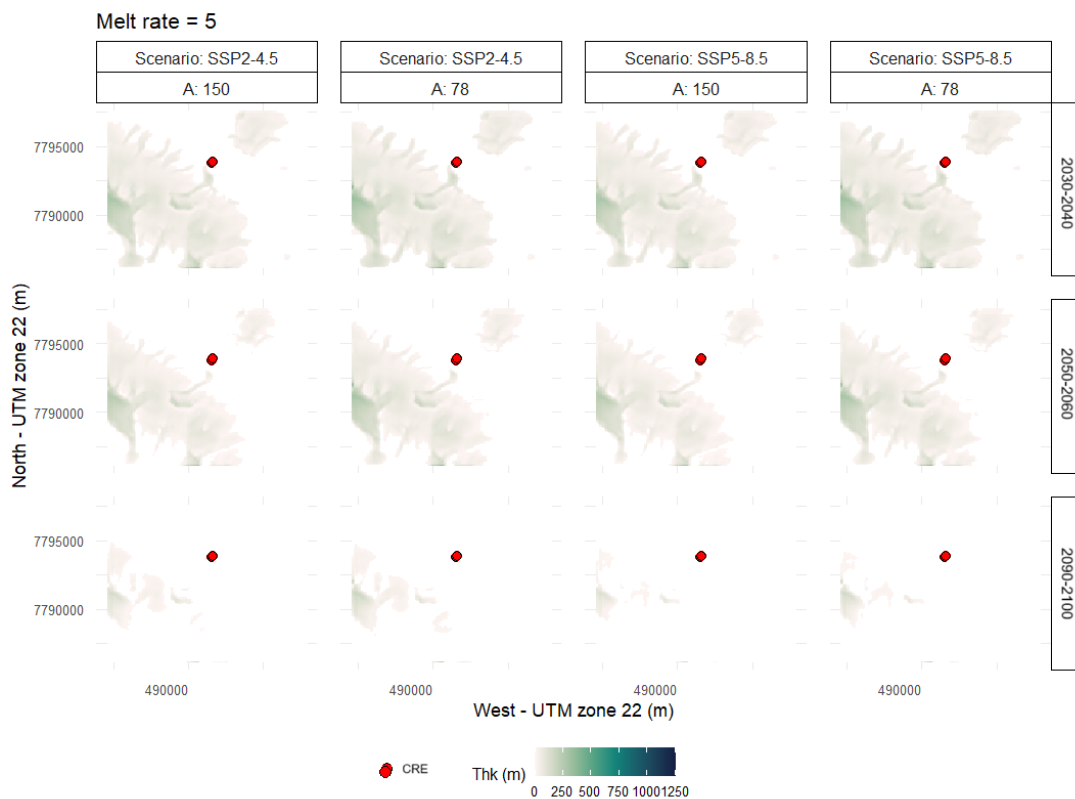


**Figure S10.** Location of the CRE samples (red dots) and average ice thickness (m) for future CMIP6 SSP2-4.5 and SSP5-8.5 scenarios and different temporal periods. The ice thickness values shown are the result of performing a spin-up model run reaching steady state conditions,

and subsequently performing a model run with CMIP6 projections from present-day to 2100. Data are shown for the calibrated melt rate (5) and calibrated IGM configuration ( $A = 150 \text{ MPa}^{-3} \text{ a}^{-1}$ ,  $c = 0.03 \text{ km MPa}^{-3} \text{ a}^{-1}$ ) as well as IGM default configuration ( $A = 78 \text{ MPa}^{-3} \text{ a}^{-1}$ ,  $c = 0.03 \text{ km MPa}^{-3} \text{ a}^{-1}$ ).

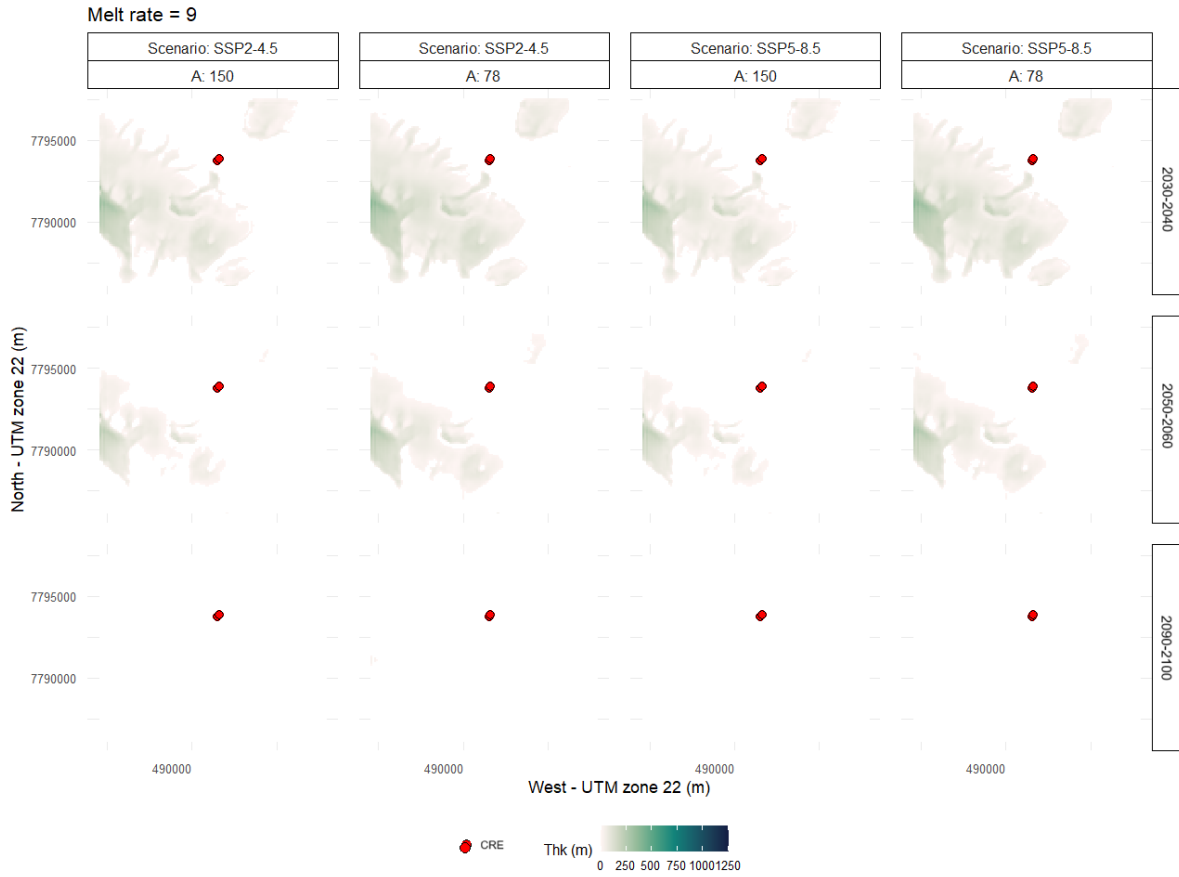


**Figure S11.** Location of the CRE samples (red dots) and average ice thickness (m) for future CMIP6 SSP2-4.5 and SSP5-8.5 scenarios and different temporal periods. The ice thickness values shown are the result of performing a spin-up model run reaching steady state conditions, and subsequently performing a model run with CMIP6 projections from present-day to 2100. Data are shown for the high-end melt rate (9) and calibrated IGM configuration ( $A = 150 \text{ MPa}^{-3} \text{ a}^{-1}$ ,  $c = 0.03 \text{ km MPa}^{-3} \text{ a}^{-1}$ ) as well as IGM default configuration ( $A = 78 \text{ MPa}^{-3} \text{ a}^{-1}$ ,  $c = 0.03 \text{ km MPa}^{-3} \text{ a}^{-1}$ ).